ACS APPLIED ENERGY MATERIALS

www.acsaem.org Article

# Physicochemical Properties of ECS Supports and Pt/ECS Catalysts

Michael J. Dzara,[⊥] Andres O. Godoy,[⊥] Madeleine Odgaard, Barr Zulevi, Alexey Serov,* Jasna Jankovic,* and Svitlana Pylypenko*

Cite This: *ACS Appl. Energy Mater.* 2021, 4, 9111−9123 Read Online

ACCESS | Metrics & More | Article Recommendations | Supporting Information

**ABSTRACT:** As polymer electrolyte membrane fuel cell technologies see increased use in the transportation and energy sectors, there continues to be a need to produce tunable, high-performance oxygen reduction reaction (ORR) catalysts. This work represents the first detailed investigation of commercially available mesoporous nitrogen-functionalized carbon supports with tunable properties (Engineered Carbon Supports, ECS) and ORR catalysts based on platinum nanoparticles (Pt-NPs) supported on these ECS materials produced by Pajarito Powders, LLC. The ECS materials with tunable concentrations of oxygen and nitrogen functional groups and varied carbon graphitization levels were investigated. First, the physicochemical properties of these Pt/ECS catalysts are presented, alongside their bare, Pt-free ECS analogue carbon support materials as investigated through a combination of characterization techniques. This yields a comprehensive catalog of physicochemical properties, including surface area, the concentration of surface dopants (nitrogen and oxygen), evaluation of graphitic content, morphology, and Pt-NP particle size distribution. Then, the ORR performance of the three different Pt/ECS catalysts in membrane electrode assemblies (MEAs) tested under low-relative-humidity conditions is presented as an example of the performance that can be obtained with these materials. All catalysts demonstrated very promising ORR performance at low relative humidity, achieving current densities between 1.8 and 1.3 A/cm$^2$ at 0.6 V. This work demonstrates that carbon supports with engineered morphologies and compositions achieved through the VariPore synthetic technology developed by Pajarito Powders, LLC are a promising platform to produce supports and catalysts with tunable properties for a variety of applications.

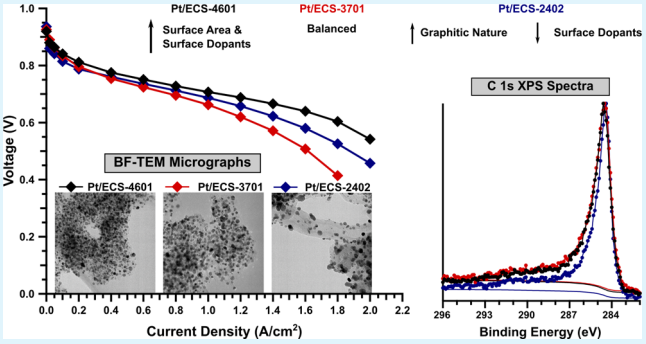


**KEYWORDS:** *platinum nanoparticle catalysts, nitrogen-doped carbon supports, ORR, transport performance, physicochemical characterization, VariPore synthesis*

## 1. INTRODUCTION

Polymer electrolyte membrane fuel cells (PEMFCs) have been the subject of intense research and development efforts over the past several decades as they are a critical component to a sustainable, hydrogen-based energy sector.[1] While commercial PEMFCs are currently available and in use in transportation and energy applications, continued improvements in PEMFC performance are desirable to drive down the cost of widespread commercial adoption.[2] Numerous studies have been devoted to the development of catalysts for the cathodic electrocatalytic oxygen reduction reaction (ORR) due to its slower kinetics, relative to the anodic hydrogen oxidation reaction.[2,3] Platinum (Pt)-based materials in which Pt-nanoparticles (Pt-NPs) are dispersed on commercially available carbon black supports with different surface areas are the state-of-the-art, and many efforts have focused on improving the catalytic activity of the Pt by tuning its physicochemical properties through a variety of routes.[2−4] This includes controlling Pt morphology and nanostructure through modification of nanoparticle shape and surface properties, altering the electronic structure through alloying, dealloying and defect formation, and other novel approaches.[5−8]

The properties of the carbon support also have a significant impact on many performance metrics of the catalysts when it is integrated into a catalyst layer for testing and used in a membrane electrode assembly (MEA).[9−12] The carbon support facilitates the dispersion of metal nanoparticles and is included to provide electrical connectivity and conductivity to the electrode. The porous network of Pt/C agglomerates drives the formation of a beneficial three-dimensional (3D) electrode structure that both brings the catalyst into contact with reactants (high catalyst utilization) and enables the necessary mass transport of products and reactants. Carbon

Received: May 14, 2021
Accepted: August 10, 2021
Published: August 24, 2021

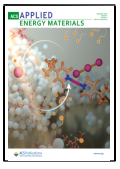






https://doi.org/10.1021/acsaem.1c01392
*ACS Appl. Energy Mater.* 2021, 4, 9111−9123

surface chemistry affects both catalyst and proton-conductive ionomer distribution, significantly affecting PEMFC performance. To deliver these requisite properties, a carbon support must have high electrical conductivity, high surface area, and a structure that provides easy access to active sites and is stable under operation conditions.[13−15] This makes carbon black and high surface area carbon (HSC) good support options, and several common commercially available carbons (Vulcan XC-72R, Ketjenblack, etc.) have often been used in Pt-based MEAs. Such particle-based carbon supports have been commercially available for over a decade and have been well studied, both in terms of physicochemical characterization and electrochemical qualities.[16,17]

It is well known that the stability of carbon-supported Pt-based catalysts is affected by both the metal catalyst and carbon support. Carbon structures are often prone to oxidation in the acidic medium at higher potentials (>1.2 V) seen during fuel cell stack start-up and high-stress operating conditions. Moreover, Pt is known to promote and accelerate undesirable degradation processes.[18−20] This necessitates the consideration of a carbon support's resistance to surface oxidation and resistance to Pt-NP migration and agglomeration, which can be enhanced by favorable catalyst−support interactions. Recently, carbon nanostructures such as carbon nanotubes, graphene, and others have been investigated as alternatives with improved corrosion stability and power density in MEA testing.[9,21,22] It has been shown that tuning the surface area and porosity, degree of graphitization, and the concentration and identity of surface defects and functional groups on the support can result in improved electrochemically active surface area (ECSA), better Pt-NP dispersions, and favorable electronic interactions between the catalyst and support.[10,11,23,24] Considering surface concentration of oxygen, a higher oxygen concentration on the surface of the support has been suggested to result in favorable catalyst−support interaction and can facilitate the formation of a catalyst layer architecture well suited for water transport. Conversely, it has been shown that a higher concentration of oxygen heteroatoms within a carbon support can have detrimental effects on the overall stability of a catalyst, and so in the case of certain properties, tradeoffs exist and optimization can be convoluted.[25,26] In a study on Pt-NP catalysts supported by commercial Vulcan XC-72R carbon black, the sample with an elevated oxygen concentration produced through a mild acid treatment showed a more severe performance loss during electrochemical durability testing. This was attributed to, in part, an increase in average Pt-NP size after testing and an increase in the oxide character of the Pt-NPs observed for the catalyst with a more heavily oxidized carbon support.[25] This further emphasizes the importance of controlling multiple properties of a novel carbon support material to foster the formation of beneficial catalyst−support interactions.

A promising avenue to tune carbon support properties is through functionalization or doping with nitrogen and/or other heteroatoms.[27] Modification of carbon supports by nitridation has been employed in various carbon structures and was evaluated for multiple electrochemical reactions. It has been shown that inclusion of N dopant atoms in a carbon structure can alter the electronic structure of the carbon matrix, changing the nature of catalyst−support interactions. An abundance of different synthetic routes for producing and/or modifying carbon support materials with nitrogen have been explored—researchers have found success with solution-based reactions, vapor deposition and growth techniques, heat treatment of existing carbon materials in reactive or inert atmospheres, and many other approaches.[14,27−29] Each synthetic scheme is likely to have tradeoffs among the various important properties of a support, such as surface area, pore-size distribution, structure, graphitization, overall nitrogen concentration and distribution, and relative proportion of different functionalities. While this may enable selection of one synthesis approach over another appropriate for a given catalytic system and reaction, many studies have shown that the more favorable catalyst−support interaction characteristic of nitrogen-functionalized carbon will generally result in improved Pt-NP dispersion and stability and in some instances increased catalytic activity relative to an undoped control.[28,30−32] Indeed, a prominent study on model nitrogen-doped highly oriented pyrolytic graphite (HOPG) substrates modified via ion implantation provided direct evidence that the proximity of metal nanoparticles to areas of high-nitrogen-dopant concentration correlated to less change in particle shape and dispersion after cycling. Better overall durability in an MEA was observed for the Vulcan black doped with nitrogen using the same nitrogen incorporation method.[31−33]

This work represents the first detailed characterization study of a relatively new (on the market for fewer than 5 years) set of commercially available mesoporous carbon supports with tunable properties known as Engineered Catalyst Support (ECS) materials produced by Pajarito Powder, LLC using their VariPore technology.[34] The ECS materials have tunable concentrations of oxygen and nitrogen functional groups and varied carbon graphitization levels. Additionally, the ECS mesoporous supports are also produced as a full catalyst decorated with Pt-NPs (Pt/ECS), with a platinized catalyst corresponding to each of the three ECS materials featured in this study also investigated. The ECS materials and the Pt/ECS catalysts supported on these carbons were studied using a comprehensive suite of physicochemical characterization techniques and tested for fuel cell performance in MEAs. X-ray diffraction (XRD) and Raman spectroscopy were used to evaluate the structural properties of the materials. Thermogravimetric analysis (TGA) measurements were performed to evaluate the thermal oxidation behavior of the supports and catalysts. X-ray photoelectron spectroscopy (XPS) was applied to investigate the relative surface concentrations and surface states of the carbon support and Pt-NPs as well as that of oxygen and nitrogen heteroatoms present. $N_2$-sorption experiments were conducted to estimate the surface area and pore-size distribution of all materials, while high resolution-transmission electron microscopy (HR-TEM), combined with energy dispersive spectroscopy (EDS), was used to further investigate morphological, structural, and compositional properties of the bare ECS supports and to analyze Pt-NP dispersion and particle size distribution. The three Pt/ECS materials were incorporated into 50 $cm^2$ MEAs and tested at 30% relative humidity (RH) to provide an initial demonstration of ORR performance. The results of this work reveal the differences in surface area, surface concentration of oxygen and nitrogen dopants, and degree of graphitization present in the bare support materials, indicating the ability to tune a catalyst's properties through modification of the support to better perform for a certain set of electrochemical conditions.


https://doi.org/10.1021/acsaem.1c01392
ACS Appl. Energy Mater. 2021, 4, 9111−9123

## 2. EXPERIMENTAL SECTION

**2.1. Catalysts.** Three commercially available ECS materials, identifiable as ECS-4601, ECS-3701, and ECS-2402, with varied content of oxygen and nitrogen functional groups were produced by Pajarito Powder, LLC using their VariPore technology.[34] Each support material was also platinized resulting in 50 wt. % Pt/ECS-4601 and Pt/ECS-3701 and 40 wt. % Pt/ECS-2402.

**2.2. Physicochemical Characterization.** Raman Spectroscopy was carried out using a Thermo DXR2 Raman spectrometer equipped with a 532 nm laser. Three scans were collected and averaged for a glass vial filled with powder, while a standard background subtraction was used to remove the glass vial contribution.

Characterization of the crystal structures and graphitic nature of the samples was performed using XRD on a Rigaku MiniFlex 600 (Rigaku Co., Japan) with monochromated Cu K$\alpha$ radiation ($\lambda$ = 1.5406 Å) and a shallow sample dish.

The pore properties of all samples were analyzed using physical adsorption of nitrogen at the liquid-nitrogen temperature (77 K) on a Micromeritics ASA P2020 Accelerated Surface Area and Porosimetry Analyzer. Prior to measurements, ECS samples were degassed at 573 K for 6 h under vacuum and Pt/ECS samples were degassed at 493 K for 6 h under vacuum. The specific surface areas were acquired using the Brunauer–Emmett–Teller (BET) method, based on a model of monolayer–multilayer adsorption, with a relative pressure range of ~0.1–0.15. Since the BET model fails to accurately describe adsorption in micropores,[35] the volume and sizes of the pores were calculated using the Barrett–Joyner–Halenda (BJH) method for the adsorption branches. The maximum positions of the BJH curves were used to estimate pore-size distributions and the volume of nitrogen adsorbed at a $P/P_o \sim 0.99$ was used to calculate the total pore volumes.

The thermal oxidation behavior of the samples was investigated using TGA. These experiments were carried out utilizing the Netzsch STA 449 F1 Jupiter Simultaneous TGA/DSC Thermal Analyzer system. Measurements were conducted using about 20 mg of the sample. The samples were heated up to 1573.15 K (1300 °C) at a rate of 10 °C/min, with an air flow of 10 mL/min.

XPS measurements were performed using a Scienta-Omicron HiPP-3 system equipped with an R4000 hemispherical analyzer energy calibrated to the Au $4f_{7/2}$ region at 83.95 eV of a sputter-cleaned Au foil. Measurements were collected with the high-voltage lenses in the Swift Acceleration operating mode, described elsewhere.[36] An Al K$\alpha$ X-ray source was operated at 300 W with an ~900 $\mu$m spot size, and all core level measurements were performed at a combination of a 200 eV pass energy and a 0.8 mm × 30 mm slit size resulting in an estimated energy resolution of 0.6 eV. Analysis chamber pressure was maintained at a level below $5.0 \times 10^{-8}$ mbar, while analyzer pressure remained below $1 \times 10^{-9}$ mbar. Samples were mounted on conducting carbon tape and therefore no charge referencing was necessary. For each sample, two separate areas of analysis were measured at identical conditions and length of measurement to verify sample homogeneity. Having confirmed that minimal variations between the areas of analysis exist, the spectra were summed to obtain the spectra displayed in this work. The measurement settings (energy range, step size, dwell time, and the number of sweeps) for each core level were kept constant from sample to sample. Spectral processing was performed in CasaXPS software, where a Shirley background was applied to all core levels. Area ratios reported were calculated without intensity calibration and therefore only accurately represent the relative change from sample to sample and are not atomic percentages.

TEM of the powder samples was conducted using a Thermo Scientific Talos F200X 200 kV D6329 XTwin TEM, using both bright field (BF) and high angle annular dark field (HAADF) scanning imaging. The samples were first dispersed in 50–50 volume percent of isopropyl alcohol (IPA) and distilled water, then ultrasonicated for 15–30 min, and finally deposited on a 200-mesh holey carbon-coated copper grid (Ted Pella Inc.) for TEM characterization after being dehydrated for 30 min under an ultraviolet lamp. EDS was performed with a ChemiSTEM technology system attached to the TEM for elemental analysis, using the hypermapping collected by an ESPRIT Microanalysis Software. The mapping was performed using the screen current of 2.5 nA, the beam dwell time of 1000 $\mu$s, and 1 mapping cycle. Pt particle size analysis was performed in ImageJ, using 200 particles for each sample, imaged by HR-TEM at 190kx magnification.

**2.3. MEA Fabrication and Testing.** MEAs with a 50 $cm^2$ active area were fabricated by IRD Fuel Cells, LLC using their proprietary industrial CCM manufacturing method. Testing was performed at 80 °C, with 2.5 bar absolute pressure, 1.5 $H_2$ stoichiometry, and 50% RH on the anode side and 2.3 bar absolute pressure, 2.0 air stoichiometry, and 30% RH on the cathode side.

## 3. RESULTS AND DISCUSSION

Three commercially available mesoporous carbon supports and corresponding supported Pt-NP catalysts were produced by the Varipore method[41] by Pajarito Powder, LLC and referred to by their commercial names—ECS-4601, ECS-3701, ECS-2402, and their Pt/ECS analogues were selected for a thorough evaluation of their physicochemical properties. The supports were "engineered" to achieve: (1) varied content of oxygen functional groups (ECS-4601 > ECS-3701) with the comparable content of nitrogen functional groups and comparable graphitization level; (2) different overall (oxygen and nitrogen) functionalization level (ECS-4601 and ECS-3701 > ECS-2402); and (3) different level of support graphitization (ECS-2402 > ECS-4601 and ECS-3701). The Pt-NPs were incorporated onto the three unique ECS materials in the same fashion for each catalyst, resulting in 50 wt. % Pt/ECS-4601 and 50 wt. % Pt/ECS-3701, which are directly comparable to each other. Additionally, a 40 wt. % Pt/ECS-2402 catalyst was selected to highlight the properties of an available lower Pt loading catalyst. Each carbon support material was designed with slight variations in the synthetic process, toward the goal of producing similar catalyst materials with all-around good performance, yet with some variations in the morphology and composition as to potentially offer advantages in different environments/testing conditions. Therefore, it is expected that differences in the Pt/ECS physicochemical and electrochemical properties are most likely driven by the properties of the support.

**3.1. Bulk Characterization: XRD, Raman Spectroscopy, and TGA.** To fully understand the role that the variation in physicochemical properties of the three ECS materials has on the Pt/ECS catalyst performance in MEA testing, the bare (Pt-free) ECS samples were thoroughly characterized alongside the Pt/ECS catalysts. The degree of graphitization of the ECS and the structural properties of the Pt-NPs are first investigated with XRD (Figure 1), with the peak parameters available in Table S1. The XRD patterns of bare ECS-4601 and ECS-3701 samples are almost identical, with the presence of broad and asymmetrical peaks at a $2\theta$ value of ~23°, in addition to more symmetrical protuberances near 43° and 80°, which are designated as the graphite (002), (101), and (110) planes.[37] The third sample (ECS-2402) shows sharper and narrower peaks, at 25.7 and 42.7°, as well as lower intensity peaks at 53.1° designated as (004) and 77.7° (110). The difference in peak width and intensity, which results in the much more clearly defined graphitic plane features observed for ECS-2402, suggests that the ECS-2402 sample contains a higher degree of crystallinity and more ordered graphitic structure than the other two samples. This may affect the dispersion of Pt-NPs as well as the stability of the carbon and catalyst.



https://doi.org/10.1021/acsaem.1c01392
ACS Appl. Energy Mater. 2021, 4, 9111–9123

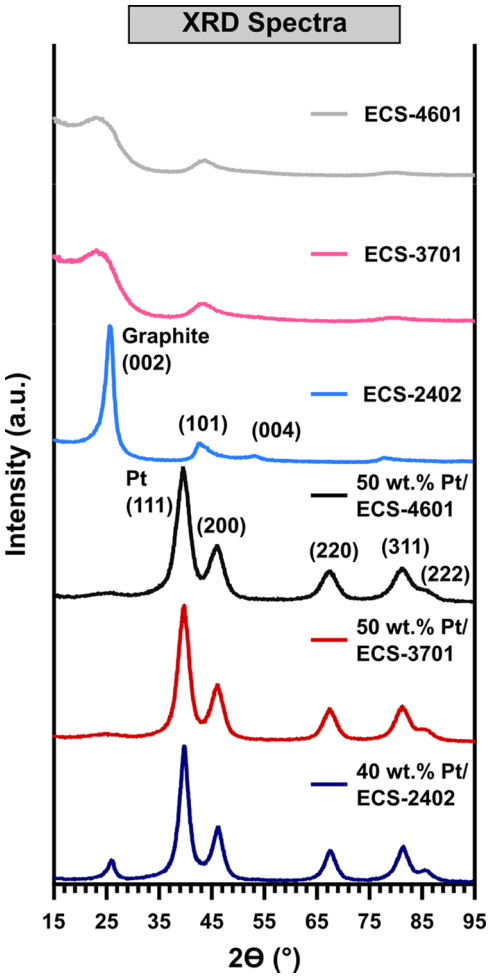


**Figure 1.** XRD patterns are displayed for all ECS and Pt/ECS materials. Major graphite and Pt planes are labeled on the plot.

Considering the XRD patterns of the Pt/ECS catalysts, the intensity of the graphite peaks is considerably reduced due to the more intense Pt peaks, with the Pt/ECS-2402 sample displaying the only clear graphitic plane feature at 25.7°. The other two samples (Pt/ECS-4601 and Pt/ECS-3701) show only a very slight bump around this position, indicating that the lower degree of graphiticity is maintained following platinization. Other than the observed difference in the graphite (002) peak, the rest of the pattern and their Pt diffraction peaks appear to be nearly identical between the three Pt/ECS samples. Although slight shifts of the diffraction peaks for all of the samples are observed, it is not straightforward to make a quantitative analysis and correlate this behavior to the characteristics and the synthesis of the samples.

The diffraction peaks observed at approximate $2\theta$ values of 39, 46, 67, 81°, and a shoulder around 85° correspond to Pt diffraction from the (111), (200), (220), (311), and (222) planes, respectively.[38] This diffraction pattern is distinctive of face-centered cubic (FCC) crystalline Pt. XRD is also used to estimate the crystallite size—defined as "L"—based on the prominent facets of the crystallites and the width of the reflection peaks of the powders. L for the Pt-NPs in each sample was calculated using Scherrer's eq 1.[39]

$$L = \frac{0.9\lambda}{\beta \cos\theta} \quad (1)$$

where $\beta$ is the full width half maximum (FWHM) of the diffraction peak in radians and the characteristic X-ray wavelength is $\lambda$ = 0.15406 nm. The Pt (220) diffraction peak is used to calculate the crystallite size because it is the least affected by the carbon support; the presence of the carbon support can result in features overlapping the broad (111) and (200) Pt peaks, making these planes less clear options. From eq 1, the samples have slightly different crystallite sizes. Pt/ECS-4601 showed the smallest crystallite size of 2.6 nm. Pt/ECS-3701, which has the same 50 wt % Pt loading as Pt/ECS-4601, showed a slightly higher crystallite size of 3.0 nm. Not surprisingly, Pt/ECS-2402 (despite having lower catalyst loading) had the highest crystallite size of 3.6 nm as the ECS-2402 has a higher degree of graphitic carbon, reducing the number of Pt anchoring sites and promoting the formation of larger crystallites. It is important to mention that crystallite size is different than particle size because one particle can be a single crystal or composed by numerous crystalline domains (crystallites) or amorphous domains. Therefore, the size of crystallites measured by XRD should be smaller than the size of particles measured by other techniques, such as TEM. Additionally, there was no evidence of other metallic phases or crystalline oxide species from XRD.

Raman spectroscopy is routinely employed to characterize graphitic carbons, as crystalline hexagonal graphite displays several prominent spectral features; (i) in the region between 1100 and 1700 $cm^{-1}$ (commonly known as the D and G bands), which is used to evaluate relative trends in the defected nature of the graphite through the ratio of their intensities ($I_D/I_G$) and (ii) second-order features between 2400 and 3300 $cm^{-1}$.[40] The Raman spectra of all three ECS samples (Figure 2) are very similar up to around 2300 $cm^{-1}$. However, sample ECS-2402 has sharper, narrower, and more clearly resolved peaks when evaluating the D and G bands at 1340 and 1570 $cm^{-1}$, respectively. Additionally, in the second-order region of the Raman spectra for ECS-2402, two peaks are present at 2690 $cm^{-1}$ (G′ band) and 2930 $cm^{-1}$ (D″ band), while only a broad, short peak centered between 2100 and 3400 $cm^{-1}$ (with one apparent maximum at 2800 $cm^{-1}$) is present for samples ECS-3701 and ECS-4601. The manifestation of the intense G′ band at 2690 $cm^{-1}$ further proves the higher degree of graphitic ordering for the ECS-2402.[41] This analysis of the Raman spectra corroborates the XRD results, further suggesting that the ECS-2402 sample is more graphitized compared to ECS-4601 and ECS-3701. For the Pt/ECS Raman spectra, essentially no major change in the Raman spectra from the respective carbon support is observed, indicating that the platinization process did not affect the structure of the host carbons.

$I_D/I_G$ ratios were calculated for all samples, and are displayed in Table S2, along with peak parameters for all samples and all features. The ratios did not show a clear trend that can express a definite relationship between the crystalline and amorphous structures of the samples. Each sample, bare or platinized, displays an intensity of the D band that is slightly higher than the G band, indicating a competitive state of amorphous and graphitic structures. Interestingly so, the values for the FWHM of the D and G peaks seemed to increase, while the peak height decreases when Pt-NPs are added. This trend regarding FWHM and peak heights indicates that the carbons were


https://doi.org/10.1021/acsaem.1c01392
ACS Appl. Energy Mater. 2021, 4, 9111−9123

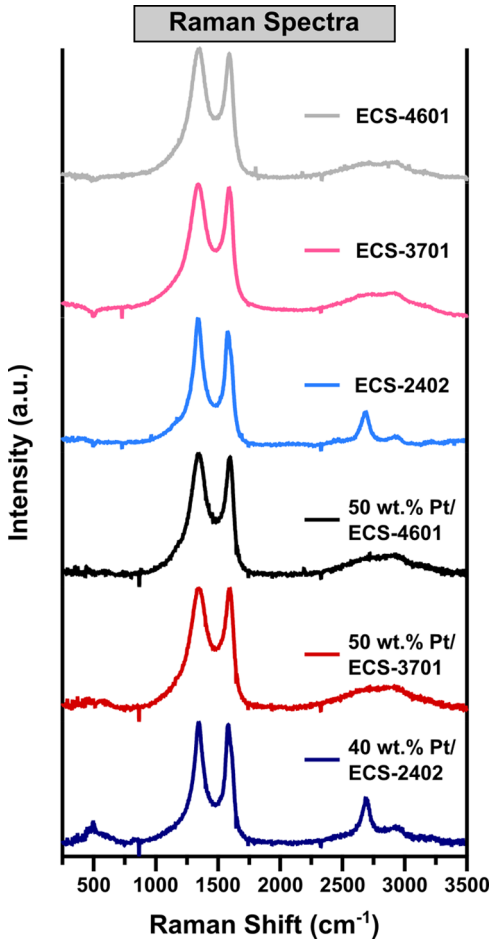


**Figure 2.** Raman spectra are displayed for all ECS and Pt/ECS materials.

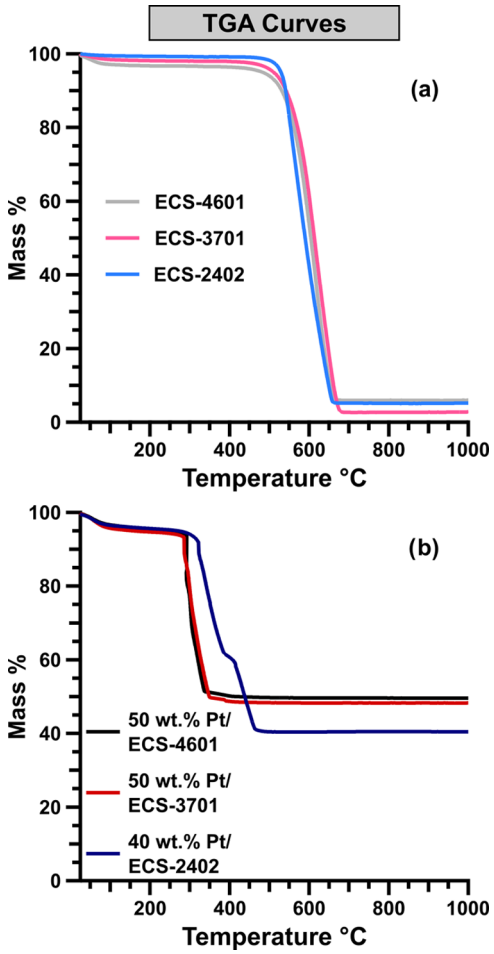


**Figure 3.** Mass loss curves collected from TGA measurements performed in air are displayed for (a) ECS materials and (b) Pt/ECS catalysts.

initially composed of small graphite sheets with some degree of graphitization but after the Pt-NP deposition on the support materials the amount of defect sites on the surface of the graphitic layer is increased, as suggested in the literature.[37,42] The FWHM value of the more graphitic ECS-2402 is smaller than the less graphitc ECS-4601 and ECS-3701, further confirming a more ordered structure (before and after Pt deposition), consistent with the XRD results.

The thermal oxidation stability of the bare support and catalyst materials was evaluated using TGA. Thermal oxidation stability of the carbon support has been correlated with electrochemical stability, specifically corrosion resistance in an operating fuel cell.[43] Figure 3 shows the weight loss vs temperature curves collected in air, and Table S3 contains the initial mass and mass retention values. Two weight loss steps were observed for all the samples. The lower-temperature step (between 25 and 150 °C) is much less prominent than the higher-temperature step, with less than 3% mass loss, most likely attributable to water loss.[44] The location of the second, main slope in the weight loss curves indicates that until about 500 °C, the samples do not undergo any significant changes. A significant oxidation took place in the second step, between 500 and 670 °C, showing almost identical degradation temperature ranges for all of the supports. For these samples, the differing degrees of graphitization observed from XRD and Raman spectroscopy did not appear to have a strong effect on the carbon oxidation and decomposition during TGA.

The Pt-NP catalysts (Figure 3b) also reveal two distinct weight loss steps, as already observed for the bare ECS materials. The presence of Pt causes the maximum rate of weight loss to occur at a temperature lower than that of the pure carbon (it accelerates the production of $CO_2$) decreasing its resistance to oxidation and accelerating carbon decomposition.[45] The two Pt/ECS materials with a lower degree of graphitization (ECS-3701 and 4601) display lower resistance to oxidation, with a significant mass loss between 280 and 350 °C. Meanwhile, in the more graphitic Pt/ECS-2402 degradation starts around 310 °C and ends around 510 °C. This is consistent with the expectation that amorphous carbon oxidizes more easily than graphitic carbon under TGA measurement conditions. However, it should also be noted that this sample has the lower weight loading of Pt, which may also impact the degradation temperature profile. Additionally, the mass percentage at which the TGA curves plateau at temperatures over 500 °C confirms the target Pt wt. % of the Pt/ECS catalysts, with Pt/ECS-4601 at 49.9%, Pt/ECS-3701 at 48.5%, and Pt/ECS-2402 at 40.7%.

**3.2. Surface Composition Analysis with XPS.** High-resolution XPS measurements of the C 1s, N 1s, and O 1s were performed to evaluate the surface composition of the bare ECS support materials (Figure 4). The C 1s is displayed with each spectrum normalized to the peak maximum value so that relative differences in peak shape are displayed. The position of


https://doi.org/10.1021/acsaem.1c01392
ACS Appl. Energy Mater. 2021, 4, 9111−9123

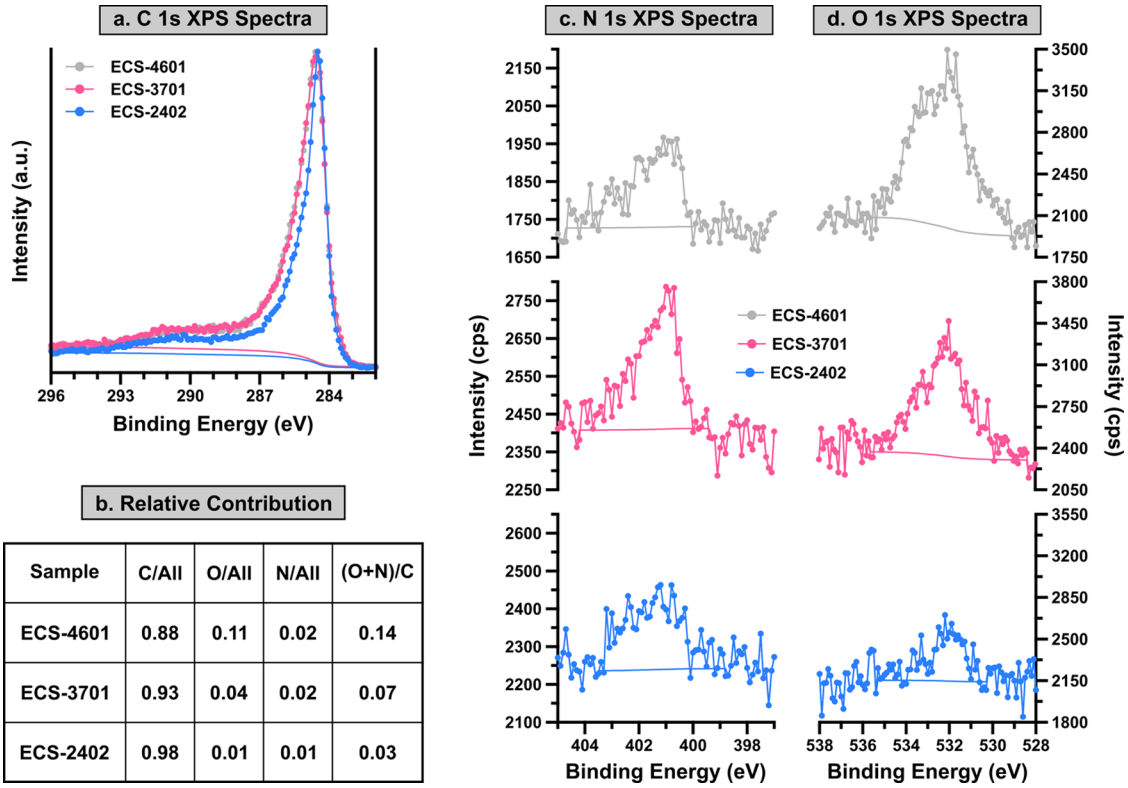


b. Relative Contribution

| Sample | C/All | O/All | N/All | (O+N)/C |
|---|---|---|---|---|
| ECS-4601 | 0.88 | 0.11 | 0.02 | 0.14 |
| ECS-3701 | 0.93 | 0.04 | 0.02 | 0.07 |
| ECS-2402 | 0.98 | 0.01 | 0.01 | 0.03 |

**Figure 4.** XPS results for the ECS materials are displayed, featuring (a) C 1s, normalized to the peak maximum value. Relative quantification (b) is shown, in which the values are calculated from the total peak areas to display relative trends in material composition, not absolute atomic percentages. The (c) N 1s and (d) O 1s are also shown, in which the y-scale is equivalent for all spectra to show relative differences in heteroatom concentration.

the peak maximum is very similar in all three samples, with 284.5 eV for ECS-3701 and ECS-2402 and 284.6 eV for ECS-4601. The value of $sp^2$-hybridized carbon such as that in graphite is typically assigned to 284.5 eV, in very good agreement with the position observed here for the three samples.[46,47] There is a clear difference in peak width however, as ECS-2402 has a narrower (FWHM = 1.0 eV) shape relative to ECS-3701 and ECS-4601 (FWHM = 1.3 eV for both). In this case, the narrower shape of ECS-2402 indicates it likely contains less defects and dopant atoms than the other two samples and perhaps less amorphous, $sp^3$-hybridized carbon.[33] Indeed, when examining the N 1s and O 1s spectra, ECS-2402 has the lowest contribution from both heteroatoms, as shown by the lower relative signal. ECS-2402 also has the lowest ratio of (O + N)/C (Figure 4b), further indicating the lowest degree of carbon functionalization. Conversely, ECS-4601 has the highest ratio of (O + N)/C, indicating that this sample has the greatest degree of functionalization. This is primarily due to ECS-4601 containing the greatest relative amount of oxygen, despite both ECS-4601 and ECS-3701 having a similar amount of nitrogen.

XPS was also used to investigate the surface state of the Pt nanoparticles. High-resolution Pt 4f spectra are shown in Figure 5 with each spectrum normalized to the $4f_{7/2}$ peak maximum value. Pt/ECS-2402 and Pt/ECS-3701 both have their peak maximum value located at a position of 71.2 eV, which is in good agreement with the $4f_{7/2}$ component for metallic Pt.[48] Pt/ECS-4601, however, has its maximum intensity at 74.5 eV, which is most likely due to larger relative contributions from PtO $4f_{7/2}$ (74.0 eV) and $PtO_2$ $4f_{7/2}$ (74.9 eV) within this sample, which also overlap with the $Pt^0$ $4f_{5/2}$ peak present at 74.5 eV. Such a difference in surface oxide content may be best explained by a difference in Pt-NP size, as any nanoparticles below ~10 nm in diameter will likely be measured in entirety by XPS. Therefore, an equivalent thickness of the oxide surface layer will have a larger relative contribution to the Pt signal as there is simply less bulk metallic Pt in a smaller nanoparticle. Additionally, Pt/ECS-4601 has a greater contribution from a high binding energy shoulder located at ~77.3 eV than the other two samples—this peak is most likely the $4f_{5/2}$ component of PtO, which occurs at 77.33 eV.[48] The C 1s of each Pt/ECS sample is also displayed (Figure 5) and shows that there are no significant changes in the C 1s upon supporting Pt nanoparticles. Each sample has a similar position and FWHM compared to their corresponding bare ECS materials, confirming that the surface of the support is not significantly altered upon supporting Pt. Additionally, no significant changes in the N 1s was observed, while a slight increase in the lower BE signal of the O 1s is present, indicative of the presence of Pt oxides/hydroxides (Figure S1).

**3.3. Morphological Properties via Physisorption Analysis and HR-TEM.** Surface area and porosity properties were investigated using $N_2$ physisorption, the isotherms of which are shown for each ECS and Pt/ECS material in Figure 6, alongside their BET surface areas (also tabulated in Table S4). Characteristic hysteresis features are present in each sample, generally located at $P/P_o$ values of approximately 0.5–0.6. The saturation level is attained at $P/P_o > 0.95$, an indication of complete pore filling in a type-IV isotherm, as well as capillary condensation occurring in both mesopore and macropore, leading to a sharp increase of nitrogen adsorption


https://doi.org/10.1021/acsaem.1c01392
ACS Appl. Energy Mater. 2021, 4, 9111–9123

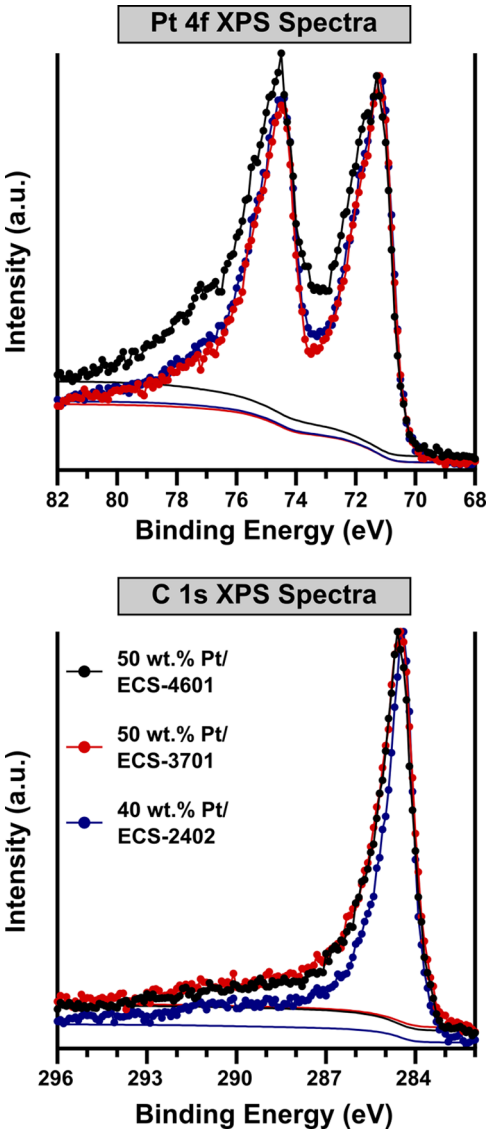


**Figure 5.** Pt 4f and C 1s spectra of Pt/ECS catalysts are displayed, with the Pt 4f normalized to the $4f_{7/2}$ peak maximum and the C 1s normalized to the region peak maximum.

and sudden rise in the isotherm.[49,50] The separation degree of adsorption and desorption curves also decreased in the same fashion, indicating that the mesopore and macropore shapes become more filled when graphitization increases in the ECS samples and with the addition of Pt-NPs, which disrupts the surfaces of these carbon supports causing a pore blockage and therefore decreasing the surface area.

The hysteresis properties within the type-IV isotherms (characteristic of mesopores) observed in all samples display a combination of H1 and H3 (with a slight tendency toward H4)-type hysteresis loops; each of these loop types is related to particular features of the pore structure and the mechanism that underline the gas adsorption.[51,52] In H1, both branches are almost vertical, parallel, and narrow over an appreciable range of gas uptake, usually observed in materials revealing a narrow range of uniform mesopores corresponding to cylinder-shaped pores. On the other hand, in H3 the loops correspond to wedge-shaped pores that are created by the piling of flaky particles and in H4 the pores are characterized by a slit shape usually found in materials with lamellar structure.[53] In terms of the shapes of these loops in the ECS samples, the bare ECS materials are mainly H1 with a tendency toward H3 that is more noticeable in ECS-2402; additionally, once Pt is loaded, the trend goes from H3 toward H4, especially in Pt/ECS-2402. These hysteresis loops are usually narrower in the Pt/ECS catalysts (having smaller pore volume) than the bare ECS materials (having larger pore volume). These observations suggest the dominance of wedge-shaped pores along with some slit-shaped pores and a transition from having perhaps well-developed cylinder-shaped pores (steeper adsorption branch) in carbons with a more disordered structure, toward slit-shape pores in the samples with more graphitic structure. These tendencies also correlate with the considerable decrease in BET surface area and the dimensions of the mesopore (surface area and volume) both when going from the more amorphous (ECS-4601 and 3701) to the more structured graphitic ECS-2402, as well as when going from bare ECS structure to the Pt-NP loaded catalysts (Figure 6). This is probably caused by (i) the slight shrinkage of the graphitic framework, confirmed by XRD with the reduction of the d-spacing between the graphitic sheet (Table S1), (ii) the rearrangement of carbon atoms in the graphitic carbon structure, (iii) the reduction of the pore volume caused by the crystallization of carbon, and (iv) the coverage or blockage of pores by Pt-NPs, suggesting that some portion of the Pt-NPs rest in or over the opening of similarly sized pores.[37]

Pore-size distributions calculated from the BJH model are displayed in Figure 6. A note that pores are generally nominated by size as micro- (<2 nm), meso- (2−50 nm), and macro- (>50 nm) by IUPAC.[54] Both ECS-4601 and ECS-3701 contain very similar, nearly bimodal distributions with one major peak around a 5−15 nm diameter at the fine mesopore scale and a second major peak at the macropore size range around 55−75 nm diameter. ECS-2402 shows a different distribution, with its main mesopore peak showing a small increase in the size of the mesopore diameter (10−20 nm) relative to the other two ECS samples and then less significant peaks in the macropore regime compared to the other two samples.

The addition of Pt does not significantly change the qualities of the PSD for the Pt/ECS-4601 and 3701 catalysts, however there is a subtle change in the case of Pt/ECS-2402. In the ECS-2402 material, the proportion of mesopores to macropores appears to slightly decrease upon supporting Pt-NPs. This suggests that there is perhaps a slight preference of Pt-NPs toward sitting in the ∼20 nm mesopore for this particular catalyst. In conclusion, even after the addition of Pt-NPs, the average size of mesopores is essentially the same, not showing a substantial change.

In summary, in all six samples, the contribution of the micropore volume is almost negligible, while mesopore volume in average accounts for almost 90%, and other 10% can be attributed to the presence of macropores. The volume ratio remains almost constant for the mesopores (with a range between 88 and 95%). The specific surface area generally decreases with the increase of pore size; specially in the samples with more graphitic carbon, having more than half of the BET surface area value of the less graphitic ones. The nanoscale porosity of the carbons examined here is indeed highly desirable for achieving high catalytic performance; it is expected to improve the dispersion of catalyst nanoparticles and facilitate the mass transfer fluxes and improve the dispersion of high active catalyst loadings.


https://doi.org/10.1021/acsaem.1c01392
ACS Appl. Energy Mater. 2021, 4, 9111−9123

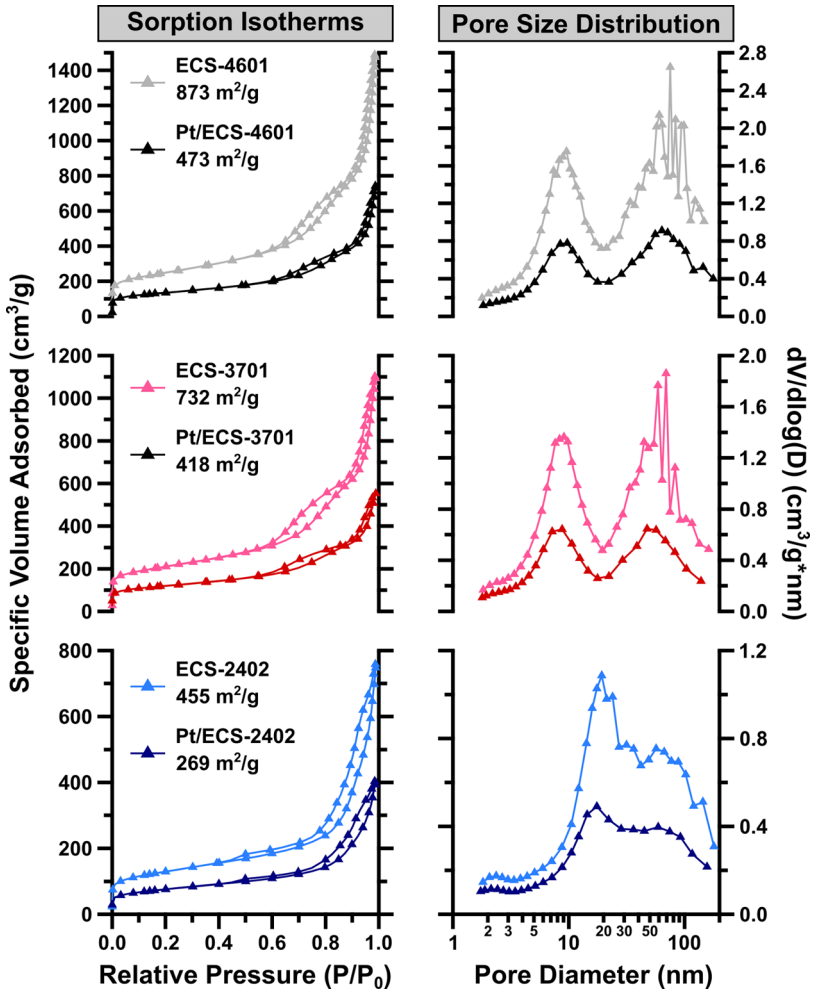


**Figure 6.** $N_2$ sorption isotherms and pore-size distribution estimated from the BJH model are displayed, alongside specific surface area values for each material estimated by the BET method.

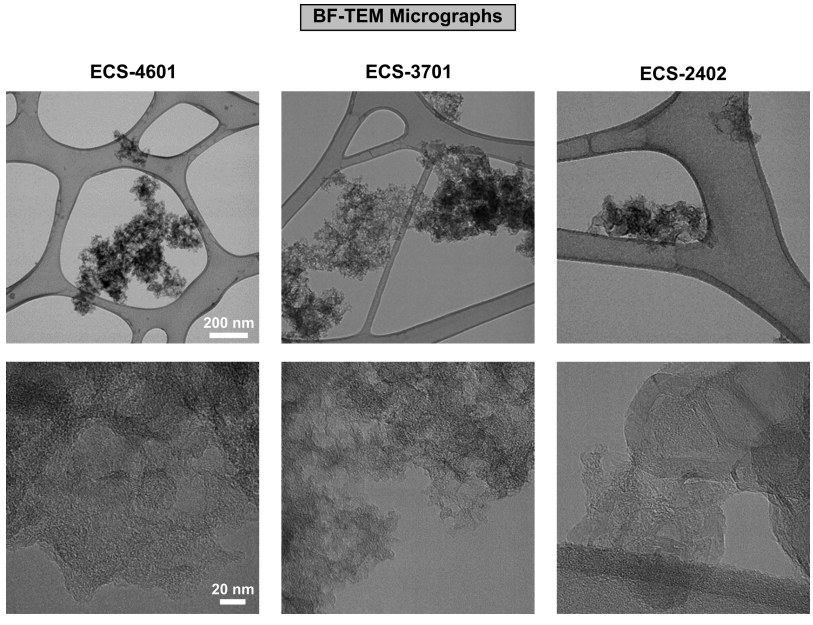


**Figure 7.** BF-TEM micrographs are displayed at lower and higher magnifications for all ECS materials.

TEM was used to investigate the morphology and structure of carbon supports and determine the distribution and size of Pt-NPs. HR-TEM micrographs in Figure 7 display the morphology of the series of bare ECS materials. The samples



https://doi.org/10.1021/acsaem.1c01392
ACS Appl. Energy Mater. 2021, 4, 9111−9123

show the presence of graphite lattice fringes, however amorphous/disordered carbon is prevalent, especially for samples ECS-3701 and ECS-4601. Sample ECS-3701 appears to contain flake-like structures from which long-range order in the form of lattice fringes is not easily discernible. The ECS-4601 sample reveals a structure fairly similar to ECS-3701 (with flake-like structures) and areas of high graphitization (with some semispherical and hollow structures). Although the images for this sample show more areas of discernable graphite fringes, it was not possible to determine the distance between the graphitic planes by TEM. In the sample with high graphitization levels (ECS-2402), the fringes in the TEM images show graphitic layers on the surface of particles that appear to look like spherical-shaped nanocarbons (or nano capsules) with a graphitic shell and a hollow interior embedded into amorphous carbon. The distance between planes in ECS-2402 was estimated to be 0.35 ± 0.005 nm, above that of equilibrium or ideal graphite phase (0.34 nm).[55] Evident from images in Figure 7, a high degree of porosity is observed in all samples.

EDS was also conducted on the three bare ECS materials (Table 1 and Figure S2). Quantification of the EDS spectra

**Table 1. EDS Quantification**

| sample ID | C/All | O/All | N/All | (O + N)/C |
|---|---|---|---|---|
| ECS-4601 | 0.92 | 0.04 | 0.03 | 0.08 |
| ECS-3701 | 0.96 | 0.02 | 0.03 | 0.04 |
| ECS-2402 | 0.95 | 0.03 | 0.02 | 0.05 |

was performed to evaluate the ratio of oxygen and nitrogen heteroatoms to the carbon structure, to complement the XPS data shown in Figure 4b. Slightly different trends were observed in EDS than XPS and can likely be attributed to differences in sampling depth, as EDS provides information from deeper within the sample than XPS. Not surprisingly, EDS shows that all samples have a higher contribution from C and respectively a lower concentration of O. This suggests that the majority of oxygen species are present at or near the surface of the ECS materials. Trends in the relative nitrogen ratios are very similar in EDS to those obtained from XPS, suggesting that the N dopants are indeed incorporated throughout the material.

TEM images of the Pt/ECS catalysts are displayed in Figure 8, primarily to evaluate Pt-NP size and distribution (Figure 9).

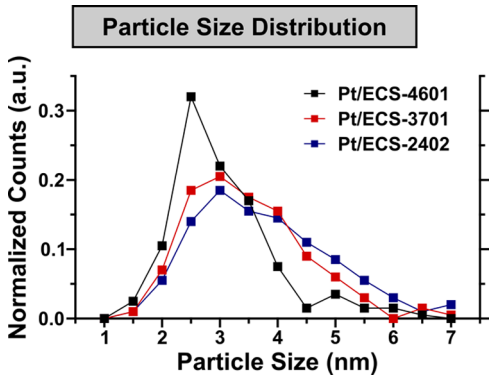


**Figure 9.** Pt-NP size distribution is displayed for all Pt/ECS catalysts, as determined by manual measurement of 200 representative Pt-NPs from BF-TEM images.

Optimal ORR activity has been suggested to be linked to Pt-NPs particles with a diameter around 3 nm, even though on average the particle size typically ranges between 1 and 10 nm, following a gaussian-type distribution. The average size of the Pt-NPs can depend on the overall loading of Pt, the type of the carbon support, and the synthesis method. Generally, a high Pt loading and carbon supports with low surface areas can lead to larger Pt-NPs. TEM micrographs of the Pt/ECS samples show a relatively uniform distribution of the quasi-spherical Pt-NPs. The average size distribution was estimated by manually measuring the diameters of 200 Pt-NPs (for each sample, respectively). Average particle sizes are 3.2 ± 1.0 nm for Pt/ECS-3701, 2.8 ± 0.9 nm for Pt/ECS-4601, and 3.5 ± 1.2 nm

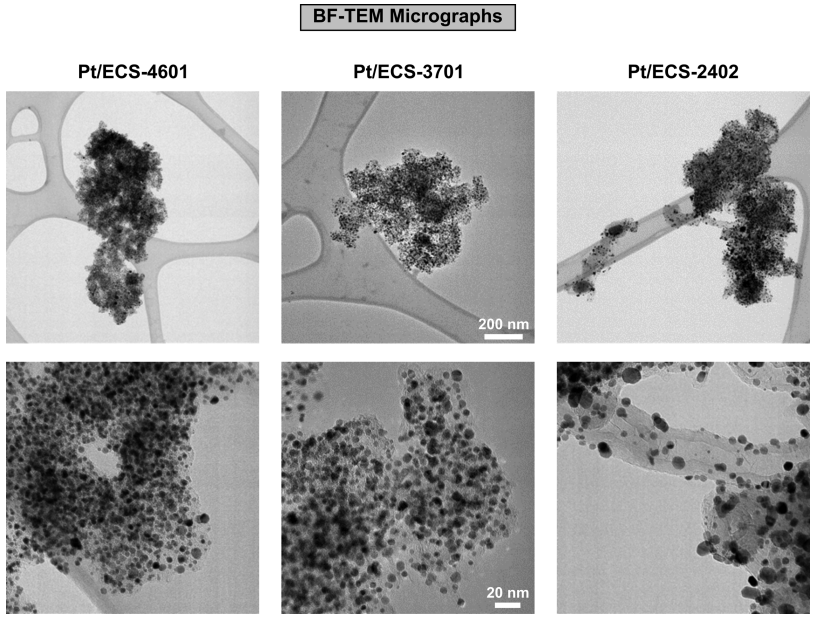


**Figure 8.** BF-TEM micrographs are displayed at lower and higher magnifications for all ECS materials.



https://doi.org/10.1021/acsaem.1c01392
ACS Appl. Energy Mater. 2021, 4, 9111−9123

for Pt/ECS-2402. These sizes are in good agreement with the crystallite sizes determined by XRD (Table S1).

Overall, the three catalysts show homogeneous distributions of Pt on the support material. Interestingly, Pt-NPs in the Pt/ECS-2402 appear to not only be uniformly deposited on the outer surface but they also seemed to be deposited on the inside of the hollow structures that this particular carbon has. Such a result implies that the multilayered graphitic structure is open and able to host the Pt-NPs. In general, the particles are homogeneous and highly dispersed on the carbon support, with the presence of some Pt-NP agglomerations. Interestingly, the shape of the Pt-NPs on the ECS-2402 appears to be more faceted or elongated than on the other substrates.

Scanning transmission electron microscopy (STEM)/EDS mapping was also used to further investigate the compositional distribution of the nanoparticles in the powder catalyst (Figure S2). It is apparent that Pt/ECS catalysts show the expected presence of Pt signal where nanoparticles are present and all samples have a generally uniform N distribution.

**3.4. MEA Performance.** The ORR catalytic properties of the three Pt/ECS catalysts were evaluated by measuring their performance in MEAs. The Pt/ECS catalysts were tested using large-area electrodes (50 $cm^2$) to demonstrate performance at a commercially relevant scale. Testing was performed in a low RH environment, which stresses transport performance and demands effective catalyst integration into the catalyst layer of the MEA.[11,56]

The resulting polarization curves are shown in Figure 10. Considering first the two catalysts with the same loading of Pt

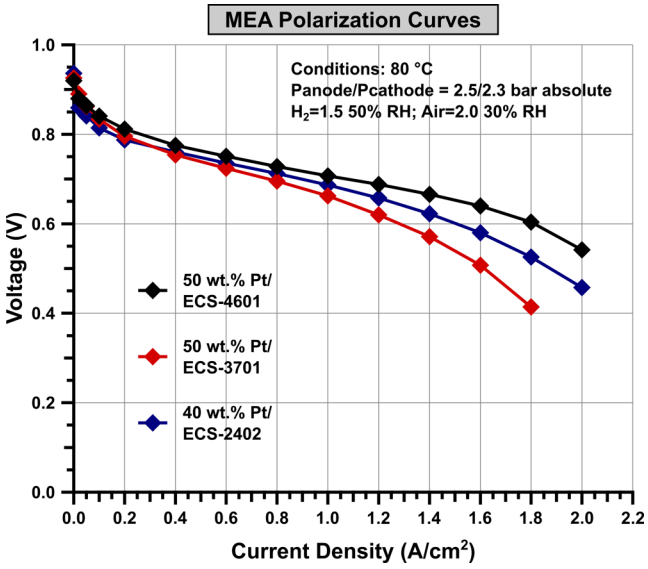


**Figure 10.** MEA polarization curves are displayed for each of the three Pt/ECS catalysts.

(50 wt. % Pt), the kinetic performance of Pt/ECS-4601 and 3701 is very similar. However, this trend does not hold when examining the mixed and mass transport limited regimes. At voltages of ~0.8 V and lower, Pt/ECS-4601 begins to display higher current density values than Pt/ECS-3701, which continues throughout the polarization curve, resulting in an ~0.5 A/$cm^2$ difference (~1.8 A/$cm^2$ for Pt/ECS-4601 vs. ~1.3 A/$cm^2$ for Pt/ECS-3701) in current density at a voltage of 0.6 V. The performance of the 40 wt. % Pt catalyst (Pt/ECS-2402) is considered next—this MEA has a marginally lower current density in the kinetic region than the other two catalysts, as expected due to its lower Pt loading. However, at voltage values below 0.8 V, the Pt/ECS-2402 catalyst begins to show higher current density values than the Pt/ECS-3701 catalyst despite its lower Pt loading. Through the transport regime, Pt/ECS-2402 maintains a higher current density than Pt/ECS-3701, resulting in a current density of ~1.5 A/$cm^2$ at 0.6 V—~0.2 A/$cm^2$ higher than Pt/ECS-3701 and ~0.3 A/$cm^2$ lower than Pt/ECS-4601. This result is an exciting initial demonstration of ORR performance in demanding operating conditions.

We now summarize the findings from the various characterizations conducted on both bare carbons and catalysts prepared with these support materials and discuss them in the context of ORR performance discussed in the previous section. We expect that the most likely parameters that are responsible for the differences in the performance of Pt/ECS-4601 and Pt/ECS-3701 at the high current density region, where mass transport plays an important role, are the catalyst surface area, surface chemistry (dopant concentration), and morphology of the bare ECS materials. Prior work has suggested that the carbon support morphology and surface area can drive the specific properties of the catalyst layer when an MEA is fabricated.[9,10] While there is a more significant set of differences between Pt/ECS-2402 and the other two catalysts, Pt/ECS-2402 is distinguished by its lower surface area and dopant concentration (with respect to both oxygen and nitrogen) and its markedly different graphitic character. ORR performance of Pt/ECS-2402 at higher current densities demonstrates strong transport performance for a catalyst at a lower Pt weight loading. This demonstrates that it is possible to maintain a high level of performance with these lower-surface-area materials, and in general, it is possible to effectively tune the properties of the ECS support materials to suit a particular testing application.

## 4. CONCLUSION AND OUTLOOK

Three commercially available mesoporous carbon support materials and their Pt-NP-decorated catalyst analogues produced by a VariPore synthetic scheme were thoroughly characterized. Each material was analyzed by a variety of techniques, yielding a bounty of physicochemical information. This shows that the ECS-4601 material has both the highest BET surface area as well as the highest concentration of surface dopants (O and N, as revealed by XPS), while XRD, Raman, XPS, and TEM all demonstrate that ECS-2402 has the largest degree of graphitization. The characterization of ECS-2402 suggests that this catalyst support may have good resistance to harsh application environments and may have the greatest longevity due to the stability and favorable properties of a graphitic support. All three Pt/ECS catalysts show very competitive transport performance in low RH testing, demonstrating that MEAs featuring Pt/ECS catalysts form a very favorable electrode structure for operation in demanding conditions. Differences in performance were observed, showing that variations in the synthesis process produced support materials with different properties, resulting in differences in mass transport properties as reflected in the performance at high current densities. The tunability of surface area and nitrogen and oxygen dopants not only provides ways to obtain good dispersions of the catalyst but also provides means to tune interactions with the ionomer and water to optimize performance for specific conditions. An additional benefit of


https://doi.org/10.1021/acsaem.1c01392
ACS Appl. Energy Mater. 2021, 4, 9111−9123

the highly graphitized supports with nitrogen heteroatoms is that they may provide improved durability of this family of catalysts, which is also the subject of future work. Overall, this work presents the highly competitive ORR performance of a set of commercial catalyst materials and demonstrates the ability to tune the properties and performance of the catalyst through variation of the support properties. Such a platform represents a promising avenue toward producing different catalysts for varied applications with favorable properties by tuning the properties of the support.

## ■ ASSOCIATED CONTENT

### Supporting Information

The Supporting Information is available free of charge at https://pubs.acs.org/doi/10.1021/acsaem.1c01392.

Table of XRD pattern parameters and associated discussion; table of Raman spectra peak parameters; table of the TGA results; N 1s and O 1s XP spectra for Pt/ECS catalysts; table of the $N_2$ sorption results; EDS maps used for quantification (PDF)

## ■ AUTHOR INFORMATION


### Corresponding Authors

**Alexey Serov** − *Pajarito Powder, LLC, Albuquerque, New Mexico 87109, United States;* Present Address: Oak Ridge National Laboratory, Oak Ridge, Tennessee 37830, United States; Email: serova@ornl.gov

**Jasna Jankovic** − *Institute of Materials Science, University of Connecticut, Storrs, Connecticut 06269, United States*; Email: jasna.jankovic@uconn.edu

**Svitlana Pylypenko** − *Department of Chemistry, Colorado School of Mines, Golden, Colorado 80401, United States;* orcid.org/0000-0001-7982-734X; Email: spylypen@mines.edu

### Authors

**Michael J. Dzara** − *Department of Chemistry, Colorado School of Mines, Golden, Colorado 80401, United States;* orcid.org/0000-0001-8125-0586

**Andres O. Godoy** − *Institute of Materials Science, University of Connecticut, Storrs, Connecticut 06269, United States*

**Madeleine Odgaard** − *IRD Fuel Cells, LLC, Albuquerque, New Mexico 87113, United States*

**Barr Zulevi** − *Pajarito Powder, LLC, Albuquerque, New Mexico 87109, United States*

Complete contact information is available at: https://pubs.acs.org/10.1021/acsaem.1c01392

### Author Contributions

⊥M.J.D. and A.O.G. contributed equally to this work.


### Notes

The authors declare no competing financial interest.

## ■ ACKNOWLEDGMENTS

All authors acknowledge support from NSF PFI-RP award #1919280-Commercializing Active and Durable Materials and Electrodes for Fuel Cell and Electrolyzer Applications, and M.J.D. and S.P. acknowledge funding from the Colorado Energy Research Collaboratory. This work makes use of the E-XPS system at the Colorado School of Mines, which was supported by the National Science Foundation under Grant No. 1626619. A.S. and B.Z. acknowledge support from DOE EERE grant DE-EE0008821.

## ■ REFERENCES


(1) Bockris, J. A Hydrogen Economy. *Science* **1972**, *176*, No. 1323.

(2) Banham, D.; Ye, S. Current Status and Future Development of Catalyst Materials and Catalyst Layers for Proton Exchange Membrane Fuel Cells: An Industrial Perspective. *ACS Energy Lett.* **2017**, *2*, 629−638.

(3) Gasteiger, H. A.; Kocha, S. S.; Sompalli, B.; Wagner, F. T. Activity Benchmarks and Requirements for Pt, Pt-Alloy, and Non-Pt Oxygen Reduction Catalysts for PEMFCs. *Appl. Catal., B* **2005**, *56*, 9−35.

(4) Nørskov, J. K.; Rossmeisl, J.; Logadottir, A.; Lindqvist, L.; Kitchin, J. R.; Bligaard, T.; Jónsson, H. Origin of the Overpotential for Oxygen Reduction at a Fuel-Cell Cathode. *J. Phys. Chem. B* **2004**, *108*, 17886−17892.

(5) Garlyyev, B.; Kratzl, K.; Rück, M.; Michalička, J.; Fichtner, J.; Macak, J. M.; Kratky, T.; Günther, S.; Cokoja, M.; Bandarenka, A. S.; Gagliardi, A.; Fischer, R. A. Optimizing the Size of Platinum Nanoparticles for Enhanced Mass Activity in the Electrochemical Oxygen Reduction Reaction. *Angew. Chem., Int. Ed.* **2019**, *58*, 9596−9600.

(6) Strasser, P.; Kühl, S. Dealloyed Pt-Based Core-Shell Oxygen Reduction Electrocatalysts. *Nano Energy* **2016**, *29*, 166−177.

(7) Alia, S. M.; Ngo, C.; Shulda, S.; Ha, M. A.; Dameron, A. A.; Weker, J. N.; Neyerlin, K. C.; Kocha, S. S.; Pylypenko, S.; Pivovar, B. S. Exceptional Oxygen Reduction Reaction Activity and Durability of Platinum-Nickel Nanowires through Synthesis and Post-Treatment Optimization. *ACS Omega* **2017**, *2*, 1408−1418.

(8) Stamenkovic, V.; Mun, B. S.; Mayrhofer, K. J. J.; Ross, P. N.; Markovic, N. M.; Rossmeisl, J.; Greeley, J.; Nørskov, J. K. Changing the Activity of Electrocatalysts for Oxygen Reduction by Tuning the Surface Electronic Structure. *Angew. Chem., Int. Ed.* **2006**, *45*, 2897−2901.

(9) Bharti, A.; Cheruvally, G. Influence of Various Carbon Nano-Forms as Supports for Pt Catalyst on Proton Exchange Membrane Fuel Cell Performance. *J. Power Sources* **2017**, *360*, 196−205.

(10) Park, Y. C.; Tokiwa, H.; Kakinuma, K.; Watanabe, M.; Uchida, M. Effects of Carbon Supports on Pt Distribution, Ionomer Coverage and Cathode Performance for Polymer Electrolyte Fuel Cells. *J. Power Sources* **2016**, *315*, 179−191.

(11) Shinozaki, K.; Yamada, H.; Morimoto, Y. Relative Humidity Dependence of Pt Utilization in Polymer Electrolyte Fuel Cell Electrodes: Effects of Electrode Thickness, Ionomer-to-Carbon Ratio, Ionomer Equivalent Weight, and Carbon Support. *J. Electrochem. Soc.* **2011**, *158*, No. B467.

(12) Ott, S.; Orfanidi, A.; Schmies, H.; Anke, B.; Nong, H. N.; Hübner, J.; Gernert, U.; Gliech, M.; Lerch, M.; Strasser, P. Ionomer Distribution Control in Porous Carbon-Supported Catalyst Layers for High-Power and Low Pt-Loaded Proton Exchange Membrane Fuel Cells. *Nat. Mater.* **2020**, *19*, 77−85.

(13) Yu, P. T.; Gu, W.; Zhang, J.; Makharia, R.; Wagner, F. T.; Gasteiger, H. A. Carbon-Support Requirements for Highly Durable Fuel Cell Operation. In *Polymer Electrolyte Fuel Cell Durability*; Springer: New York, NY, 2009; pp 29−53.

(14) Trogadas, P.; Fuller, T. F.; Strasser, P. Carbon as Catalyst and Support for Electrochemical Energy Conversion. *Carbon* **2014**, *75*, 5−42.

(15) Uchida, M.; Park, Y. C.; Kakinuma, K.; Yano, H.; Tryk, D. A.; Kamino, T.; Uchida, H.; Watanabe, M. Effect of the State of Distribution of Supported Pt Nanoparticles on Effective Pt Utilization in Polymer Electrolyte Fuel Cells. *Phys. Chem. Chem. Phys.* **2013**, *15*, 11236−11247.

(16) Sharma, S.; Pollet, B. G. Support Materials for PEMFC and DMFC Electrocatalysts—A Review. *J. Power Sources* **2012**, *208*, 96−119.

(17) Antolini, E. Carbon Supports for Low-Temperature Fuel Cell Catalysts. *Appl. Catal., B* **2009**, *88*, 1−24.

(18) Pandy, A.; Yang, Z.; Gummalla, M.; Atrazhev, V. V.; Kuzminyh, N. Y.; Sultanov, V. I.; Burlatsky, S. A Carbon Corrosion Model to Evaluate the Effect of Steady State and Transient Operation of a Polymer Electrolyte Membrane Fuel Cell. *J. Electrochem. Soc.* **2013**, *160*, F972−F979.
(19) Kangasniemi, K. H.; Condit, D. A.; Jarvi, T. D. Characterization of Vulcan Electrochemically Oxidized under Simulated PEM Fuel Cell Conditions. *J. Electrochem. Soc.* **2004**, *151*, No. E125.
(20) Linse, N.; Gubler, L.; Scherer, G. G.; Wokaun, A. The Effect of Platinum on Carbon Corrosion Behavior in Polymer Electrolyte Fuel Cells. *Electrochim. Acta* **2011**, *56*, 7541−7549.
(21) Oh, E. J.; Hempelmann, R.; Nica, V.; Radev, I.; Natter, H. New Catalyst Supports Prepared by Surface Modification of Graphene- and Carbon Nanotube Structures with Nitrogen Containing Carbon Coatings. *J. Power Sources* **2017**, *341*, 240−249.
(22) Lee, G.; Choi, H.; Tak, Y. In Situ Durability of Various Carbon Supports against Carbon Corrosion during Fuel Starvation in a PEM Fuel Cell Cathode. *Nanotechnology* **2019**, *30*, No. 085402.
(23) Sepp, S.; Vaarmets, K.; Nerut, J.; Tallo, I.; Tee, E.; Kurig, H.; Aruväli, J.; Kanarbik, R.; Lust, E. Enhanced Stability of Symmetrical Polymer Electrolyte Membrane Fuel Cell Single Cells Based on Novel Hierarchical Microporous-Mesoporous Carbon Supports. *J. Solid State Electrochem.* **2017**, *21*, 1035−1043.
(24) Yarlagadda, V.; Carpenter, M. K.; Moylan, T. E.; Kukreja, R. S.; Koestner, R.; Gu, W.; Thompson, L.; Kongkanand, A. Boosting Fuel Cell Performance with Accessible Carbon Mesopores. *ACS Energy Lett.* **2018**, 618−621.
(25) Kim, J. H.; Cheon, J. Y.; Shin, T. J.; Park, J. Y.; Joo, S. H. Effect of Surface Oxygen Functionalization of Carbon Support on the Activity and Durability of Pt/C Catalysts for the Oxygen Reduction Reaction. *Carbon* **2016**, *101*, 449−457.
(26) Pérez-Rodríguez, S.; Pastor, E.; Lázaro, M. J. Electrochemical Behavior of the Carbon Black Vulcan XC-72R: Influence of the Surface Chemistry. *Int. J. Hydrogen Energy* **2018**, *43*, 7911−7922.
(27) Wood, K. N.; O'Hayre, R.; Pylypenko, S. Recent Progress on Nitrogen/Carbon Structures Designed for Use in Energy and Sustainability Applications. *Energy Environ. Sci.* **2014**, *7*, 1212−1249.
(28) Zhou, Y.; Neyerlin, K.; Olson, T. S.; Pylypenko, S.; Bult, J.; Dinh, H. N.; Gennett, T.; Hayre, R. O. Enhancement of Pt and Pt-Alloy Fuel Cell Catalyst Activity and Durability via Nitrogen-Modified Carbon Supports. *Energy Environ. Sci.* **2010**, *3*, 1437−1446.
(29) Wood, K. N.; Dameron, A. A.; Joghee, P.; Bender, G.; Hayre, R. O.; Pylypenko, S. Nitrogen Post Modification of PtRu/Carbon Catalysts for Improved Methanol Oxidation Reaction Performance in Alkaline Media. *J. Electrochem. Soc.* **2015**, *162*, No. F913.
(30) Pylypenko, S.; Queen, A.; Olson, T. S.; Dameron, A.; Neill, K. O.; Neyerlin, K. C.; Pivovar, B.; Dinh, H. N.; Ginley, D. S.; Gennett, T.; Hayre, R. O. Tuning Carbon-Based Fuel Cell Catalyst Support Structures via Nitrogen Functionalization. II. Investigation of Durability of Pt-Ru Nanoparticles Supported on Highly Oriented Pyrolytic Graphite Model Catalyst Supports As a Function of Nitrogen Implantatio. *J. Phys. Chem. C* **2011**, *115*, 13676−13684.
(31) Corpuz, A. R.; Wood, K. N.; Pylypenko, S.; Dameron, A. A.; Joghee, P.; Olson, T. S.; Bender, G.; Dinh, H. N.; Gennett, T.; Richards, R. M.; O'Hayre, R. Effect of Nitrogen Post-Doping on a Commercial Platinum-Ruthenium/Carbon Anode Catalyst. *J. Power Sources* **2014**, *248*, 296−306.
(32) Pylypenko, S.; Borisevich, A.; More, K. L.; Corpuz, A. R.; Holme, T.; Dameron, A. A.; Olson, T. S.; Dinh, H. N.; Gennett, T.; O'Hayre, R. Nitrogen: Unraveling the Secret to Stable Carbon-Supported Pt-Alloy Electrocatalysts. *Energy Environ. Sci.* **2013**, *6*, 2957−2964.
(33) Pylypenko, S.; Queen, A.; Olson, T. S.; Dameron, A.; O'Neill, K.; Neyerlin, K. C.; Pivovar, B.; Dinh, H. N.; Ginley, D. S.; Gennett, T.; O'Hayre, R. Tuning Carbon-Based Fuel Cell Catalyst Support Structures via Nitrogen Functionalization. I. Investigation of Structural and Compositional Modification of Highly Oriented Pyrolytic Graphite Model Catalyst Supports as a Function of Nitrogen Implantation Do. *J. Phys. Chem. C* **2011**, *115*, 13667−13675.
(34) Serov, A.; Lubers, A.; McCool, G.; McKinney, S.; Romero, H.; Zulevi, B. In *Varipore: A Powerful Manufacturing Platform for Fuel Cell and Electrolyzer Applications*, ECS Meeting Abstracts. No. 37; IOP Publishing, 2019.
(35) Weidenthaler, C. Pitfalls in the Characterization of Nanoporous and Nanosized Materials. *Nanoscale* **2011**, *3*, 792−810.
(36) Edwards, M. O. M.; Karlsson, P. G.; Eriksson, S. K.; Hahlin, M.; Siegbahn, H.; Rensmo, H.; Kahk, J. M.; Villar-Garcia, I. J.; Payne, D. J.; Åhlund, J. Increased Photoelectron Transmission in High-Pressure Photoelectron Spectrometers Using "Swift Acceleration. *Nucl. Instrum. Methods Phys. Res., Sect. A* **2015**, *785*, 191−196.
(37) Shanahan, P. V.; Xu, L.; Liang, C.; Waje, M.; Dai, S.; Yan, Y. S. Graphitic Mesoporous Carbon as a Durable Fuel Cell Catalyst Support. *J. Power Sources* **2008**, *185*, 423−427.
(38) Sharma, R.; Wang, Y.; Li, F.; Chamier, J.; Andersen, S. M. Particle Size-Controlled Growth of Carbon-Supported Platinum Nanoparticles (Pt/C) through Water-Assisted Polyol Synthesis. *ACS Omega* **2019**, *4*, 15711−15720.
(39) Li, W.; Zhou, W.; Li, H.; Zhou, Z.; Zhou, B.; Sun, G.; Xin, Q. Nano-Stuctured Pt−Fe/C as Cathode Catalyst in Direct Methanol Fuel Cell. *Electrochim. Acta* **2004**, *49*, 1045−1055.
(40) Wang, Y.; Alsmeyer, D. C.; McCreery, R. L. Raman Spectroscopy of Carbon Materials: Structural Basis of Observed Spectra. *Chem. Mater.* **1990**, *2*, 557−563.
(41) Vidano, R.; Fischbach, D. B. New Lines in the Raman Spectra of Carbons and Graphite. *J. Am. Ceram. Soc.* **1978**, *61*, 13−17.
(42) Wang, J. N.; Zhao, Y. Z.; Niu, J. J. Preparation of Graphitic Carbon with High Surface Area and Its Application as an Electrode Material for Fuel Cells. *J. Mater. Chem.* **2007**, *17*, 2251−2256.
(43) Forouzandeh, F.; Banham, D.; Feng, F.; Li, X.; Ye, S.; Birss, V. Corrosion Study of Mesoporous Carbon Supports for Use in PEM Fuel Cells. *ECS Trans.* **2013**, *58*, 1739−1749.
(44) Baturina, O. A.; Aubuchon, S. R.; Wynne, K. J. Thermal Stability in Air of Pt/C Catalysts and PEM Fuel Cell Catalyst Layers. *Chem. Mater.* **2006**, *18*, 1498−1504.
(45) Sellin, R.; Clacens, J.-M.; Coutanceau, C. A Thermogravimetric Analysis/Mass Spectroscopy Study of the Thermal and Chemical Stability of Carbon in the Pt/C Catalytic System. *Carbon* **2010**, *48*, 2244−2254.
(46) Blyth, R. I. R.; Buqa, H.; Netzer, F. P.; Ramsey, M. G.; Besenhard, J. O.; Golob, P.; Winter, M. XPS Studies of Graphite Electrode Materials for Lithium Ion Batteries. *Appl. Surf. Sci.* **2000**, *167*, 99−106.
(47) Beamson, G.; Briggs, D. *High Resolution XPS of Organic Polymers: The Scienta ESCA300 Database*; American Chemical Society, 1993; Vol. 70. https://doi.org/10.1021/ed070pA25.5.
(48) Miller, D. J.; Øberg, H.; Kaya, S.; Sanchez Casalongue, H.; Friebel, D.; Anniyev, T.; Ogasawara, H.; Bluhm, H.; Pettersson, L. G. M.; Nilsson, A. Oxidation of Pt(111) under near-Ambient Conditions. *Phys. Rev. Lett.* **2011**, *107*, No. 195502.
(49) Wang, R.; Sang, S.; Zhu, D.; Liu, S.; Yu, K. Pore Characteristics and Controlling Factors of the Lower Cambrian Hetang Formation Shale in Northeast Jiangxi, China. *Energy Explor. Exploit.* **2018**, *36*, 43−65.
(50) Sultana, K. N.; Worku, D.; Hossain, M. T. Z.; Ilias, S. Synthesis of Graphitic Mesoporous Carbon from Metal Impregnated Silica Template for Proton Exchange Membrane Fuel Cell Application. *Fuel Cells* **2019**, *19*, 27−34.
(51) Thommes, M.; Kaneko, K.; Neimark, A. V.; Olivier, J. P.; Rodriguez-Reinoso, F.; Rouquerol, J.; Sing, K. S. W. Physisorption of Gases, with Special Reference to the Evaluation of Surface Area and Pore Size Distribution (IUPAC Technical Report). *Pure Appl. Chem.* **2015**, *87*, 1051−1069.
(52) Reporting Physisorption Data for Gas/Solid Systems With Special Reference to the Determination of Surface Area and Porosity.
(53) Yang, C.; Zhang, J.; Han, S.; Wang, X.; Wang, L.; Yu, W.; Wang, Z. Compositional Controls on Pore-Size Distribution by Nitrogen Adsorption Technique in the Lower Permian Shanxi Shales, Ordos Basin. *J. Nat. Gas Sci. Eng.* **2016**, *34*, 1369−1381.

(54) Rouquerol, J.; Avnir, D.; Fairbridge, C. W.; Everett, D. H.; Haynes, J. M.; Pernicone, N.; Ramsay, J. D. F.; Sing, K. S. W.; Unger, K. K. Recommendations for the Characterization of Porous Solids (Technical Report). *Pure Appl. Chem.* **1994**, *66*, 1739−1758.
(55) Hasché, F.; Oezaslan, M.; Strasser, P. Activity, Stability and Degradation of Multi Walled Carbon Nanotube (MWCNT) Supported Pt Fuel Cell Electrocatalysts. *Phys. Chem. Chem. Phys.* **2010**, *12*, 15251−15258.
(56) Zhang, J.; Tang, Y.; Song, C.; Xia, Z.; Li, H.; Wang, H.; Zhang, J. PEM Fuel Cell Relative Humidity (RH) and Its Effect on Performance at High Temperatures. *Electrochim. Acta* **2008**, *53*, 5315−5321.



https://doi.org/10.1021/acsaem.1c01392
*ACS Appl. Energy Mater.* 2021, 4, 9111−9123